Volume 15
Number 3
21 January 2024
Pages 783–1164

Chemical Science

rsc.li/chemical-science

ISSN 2041-6539

ROYAL SOCIETY OF CHEMISTRY

EDGE ARTICLE

Yu Wang *et al.*

Engineering band structuring *via* dual atom modification for an efficient photoanode

Chemical Science

ROYAL SOCIETY OF CHEMISTRY

EDGE ARTICLE

View Article Online
View Journal | View Issue

Cite this: *Chem. Sci.*, 2024, **15**, 896

All publication charges for this article have been paid for by the Royal Society of Chemistry

Received 12th October 2023
Accepted 5th November 2023

DOI: 10.1039/d3sc05420a

rsc.li/chemical-science

Engineering band structuring *via* dual atom modification for an efficient photoanode†

Xiaodong Wang,‡[a] Huijuan Zhang,‡[ab] Chuanzhen Feng[a] and Yu Wang *[ab]

Efficient carrier separation is important for improving photoelectrochemical water splitting. Here, the morphology modification and band structure engineering of Ta_3N_5 are accomplished by doping it with Cu and Zr using a two-step method for the first time. The initially interstitially-doped Cu atoms act as anchors to interact with subsequently doped Zr atoms under the influence of differences in electronegativity. This interaction results in Cu,Zr_g–Ta_3N_5 having a dense morphology and higher crystallinity, which helps to reduce carrier recombination at grain boundaries. Furthermore, the gradient doping of Zr generates a band edge energy gradient, which significantly enhances bulk charge separation efficiency. Therefore, a photoanode based on Cu,Zr_g–Ta_3N_5 delivers an onset potential of 0.38 V_{RHE} and a photocurrent density of 8.9 mA cm^{-2} at 1.23 V_{RHE}. Among all the Ta_3N_5-based photoanodes deposited on FTO, a Cu,Zr_g–Ta_3N_5-based photoanode has the lowest onset potential and highest photocurrent. The novel material morphology regulation and band edge position engineering strategies described herein provide new ideas for the preparation of other semiconductor nanoparticles to improve the photoelectrochemical water splitting performance.

Introduction

Photoelectrochemical (PEC) or electrocatalytic (EC) water splitting, exploiting sunlight or electricity to convert water into hydrogen and oxygen, are effective ways to respond to growing global energy and environmental issues related to fossil fuel consumption.[1–7] The photoelectrode, which absorbs sunlight to generate carriers, is the core of PEC systems.[8,9] Despite a great deal of effort having been devoted to investigating photoelectrodes with high sunlight-to-electron conversion efficiency, there are still many issues with photoelectrodes.[10,11] Specifically, trap states at grain boundaries,[12] bulk recombination,[13] high onset potential[14] and low photocurrent[15] hinder the realization of a semiconductor for water splitting. Therefore, the development of photoelectrodes with excellent PEC performance is desirable.

Photoelectrodes for PEC water splitting should possess several important properties, including a small band gap to guarantee long-wavelength light absorption, efficient charge separation and catalytic activity. Tantalum nitride (Ta_3N_5), an n-type semiconductor material, is one of the most promising photoanode materials for PEC water splitting.[16–18] However, pure Ta_3N_5 exhibits inferior PEC water splitting performance, although theoretically it can produce a maximum photocurrent density of 12.9 mA cm^{-2} under standard sunlight irradiation.[19–21] Some effective strategies, such as foreign atom doping,[22,23] morphological modification[24,25] or interface engineering,[26–28] have been developed to optimize the performance of PEC water splitting, but the photocurrent of the photoelectrode deposited on FTO is far below the theoretical value.[29–33] This phenomenon is primarily related to poor carrier transport and severe trap states at grain boundaries. In particular, when operating at a low bias potential, carrier transport is highly susceptible to potential barriers within the conduction path and easy recombination at grain boundaries. Therefore, it is crucial to focus on improving the separation efficiency of the carriers. Constructing a built-in electric field is an effective way to improve charge separation.[34,35] In the conventional built-in electric field construction, heterojunctions or homojunctions are mostly effective for enhancing carrier separation. However, there are still some conceivable deficiencies that need to be properly considered.[36,37] On the one hand, it is difficult to create an effective heterojunction due to the mismatched energy levels between two semiconductors without generating a low interface defect density. Although Ta_3N_5 heterojunctions have been reported in the literature, the processes used to synthesize these materials are cumbersome and the inhibition of deep level defects is limited.[26] On the other hand, most synthesis methods for doping a material with foreign atoms to obtain homogeneous junctions, such as the dual-source electron-beam

[a]*The School of Chemistry and Chemical Engineering, National Key Laboratory of Power Transmission Equipment Technology, Chongqing University, 174 Shazheng Street, Shapingba District, Chongqing City, 400044, P. R. China. E-mail: wangy@cqu.edu.cn*
[b]*College of Chemistry and Environmental Science, Inner Mongolia Normal University, Huhehaote, 010022, P. R. China*

† Electronic supplementary information (ESI) available. See DOI: https://doi.org/10.1039/d3sc05420a

‡ These authors contributed equally to this work.

evaporation deposit method and nitriding at a high temperature,[34,38] require intricate experimental conditions, which increase costs and the difficulty of synthesis. Additionally, heteroatom doping results in the lattice expansion of the pristine semiconductor, creating lower crystallinity and a smaller grain size, which leads to carrier recombination at grain boundaries.[12] As a consequence, a new strategy needs to be proposed to prevent the grain boundaries from influencing the charge transfer properties and to improve the bulk carrier separation efficiency. To the best of our knowledge, there is no report on modifying the morphology and bandgap structure of a semiconductor through dual-heteroatom doping.

Herein, we report for the first time the preparation of Cu and gradient Zr co-doped Ta_3N_5 (Cu,Zr_g–Ta_3N_5) using a two-step synthesis strategy. Due to the electronegativity difference between Cu and Zr, the interstitially doped Cu serves as an anchor site for subsequent interaction with Zr, which modifies the morphology of Ta_3N_5. Additionally, the incorporation of Zr affects the bandgap position. Therefore, a simplified linear pressure-assisted method is used to achieve gradient Zr doping, which bends the band structure of Ta_3N_5 to form a built-in electric field. Experimental results reveal that the doping of Cu and gradient Zr suppresses the intrinsic defect-related and grain boundary recombination of Ta_3N_5. Additionally, the gradient Zr doping allows electrons to rapid transfer to the surface of Cu,Zr_g–Ta_3N_5, resulting in an onset potential of 0.38 V_{RHE}, which is approximately 0.27 V_{RHE} lower than the onset potential of pristine Ta_3N_5 ($\sim$0.65 V_{RHE}). The photocurrent density at 1.23 V_{RHE} is 8.9 mA cm^{-2}, which exceeds that of all Ta_3N_5-based photoanodes deposited on FTO. These results demonstrate that the sequential doping of two types of atoms can change the morphology of the base material, and that gradient doping can alter the bandgap structure and improve the performance of the photoanode.

Experimental

Preparation of pristine Ta_3N_5

Ta_2O_5 (99.99%, Shanghai Adamas Reagent Co., Ltd.) was well mixed with 0.5 mmol of Na_2CO_3 (99.5%, Wako Pure Chemical Industries, Ltd.) *via* mechanical grinding in an agate mortar for 0.5 h. The mixture was then heated to 900 °C for 15 h at a ramp rate of 10 °C min^{-1} under an ammonia stream (flow rate: 120 sccm). The nitridation duration of 15 h was determined by the complete transition of the intermediate phase, $NaTaO_3$ to Ta_3N_5. After being allowed to cool to room temperature naturally, the sample was rinsed with water at 65 °C and dried under vacuum at 40 °C for 5 h.

Preparation of Cu-doped Ta_3N_5 (Cu–Ta_3N_5)

The starting materials Ta_2O_5 and $Cu(NO_3)_2 \cdot 3H_2O$ (Kanto Chemical Co., Inc.) were well blended (5.3, 5.8, 6.4, 6.9, 7.5 at% doped). Then, the mixture was annealed in air at 650 °C for 0.5 h to prepare pure oxide precursors. The annealed oxide precursors were mixed with a flux of 0.5 mmol Na_2CO_3 *via* mechanical grinding in an agate mortar for 0.5 h. For nitridation, the mixed powder was placed into an alumina boat in a furnace and was subsequently heated under an NH_3 flow of 120 sccm at 900 °C for 15 h at a ramping rate of 10 °C min^{-1}. After being allowed to cool to room temperature naturally, the sample was rinsed with water at 65 °C and dried under vacuum at 40 °C for 5 h.

Preparation of Zr-doped Ta_3N_5 (Zr–Ta_3N_5)

The starting materials Ta_2O_5 and $ZrO(NO_3)_2 \cdot 2H_2O$ (Kanto Chemical Co., Inc.) were well blended (0.62, 0.78, 0.90, 1.08, 1.25 at% doped). Then, the mixture was annealed in air at 650 °C for 0.5 h to prepare pure oxide precursors. The annealed oxide precursors were mixed with a flux of 0.5 mmol of Na_2CO_3 *via* mechanical grinding in an agate mortar for 0.5 h. For nitridation, the mixed powder was placed in an alumina boat in a furnace and was subsequently heated under an NH_3 flow of 120 sccm at 900 °C for 15 h at a ramping rate of 10 °C min^{-1}. After being allowed to cool to room temperature naturally, the sample was rinsed with water at 65 °C and dried under vacuum at 40 °C for 5 h.

Preparation of gradient and homogeneous Zr-doped Cu–Ta_3N_5 (Cu,Zr_g–Ta_3N_5; Cu,Zr_h–Ta_3N_5)

The Cu,Zr_g–Ta_3N_5 powder was synthesized by heating Cu–Ta_3N_5 powder with $ZrO(NO_3)_2 \cdot 2H_2O$ powder (0.90 at% doped). Specifically, the Cu–Ta_3N_5 was well mixed with $ZrO(NO_3)_2 \cdot 2H_2O$ powder. Then, the mixture was annealed in air at 650 °C for 0.5 h to prepare pure oxide precursors. The annealed oxide precursors were mixed with a flux of 0.5 mmol of Na_2CO_3 *via* mechanical grinding in an agate mortar for 0.5 h.

The mixture was placed in a simplified linear pressure-assisted reactor under an NH_3 atmosphere. Firstly, the temperature was increased to 900 °C (10 °C min^{-1}), and then linearly pressurized from 0.12 MPa at a rate of 0.01 MPa every 10 min for 280 min, resulting in the formation of Cu,Zr_g-doped Ta_3N_5. After being allowed to cool to room temperature naturally, the sample was rinsed with water at 65 °C and dried under vacuum at 40 °C for 5 h. Cu,Zr_h–Ta_3N_5 was synthesized in the same way, but not under simplified linear pressure, and under an NH_3 flow of 120 sccm at 900 °C for 15 h at a ramping rate of 10 °C min^{-1}.

Preparation of photoanodes *via* an electrophoretic deposition method

All tested photoanodes were prepared *via* an electrophoretic deposition method (EPD) on conducting FTO glass supports. EPD was carried out in acetone (50 mL) containing the as-prepared samples (40 mg) and iodine (10 mg), which was dispersed by sonication for 10 min. Two FTO electrodes (1.6 × 2 cm^2) were immersed parallel in the solution at a distance of 10 mm, and 15 V bias was then applied between the electrodes for 3 min using a potentiostat (PARSTAT 2263, Princeton Applied Research). The coated area was controlled to be *ca.* 1.6 × 1.0 cm^2. The electrode was dried in air at room temperature. The average thickness of the as-prepared samples deposited on FTO was 3.0 μm under the EPD conditions.

Preparation and loading of the NiCoFe–B_i co-catalyst

The preparation and loading of the NiCoFe–B_i co-catalyst was based on previous literature.[39] Specifically, the as-prepared electrodes were transferred to an Ar-purged solution containing 2 mM $NiSO_4 \cdot 6H_2O$ (99.99% metals basis, Chengdu Chron Chemical Co., Ltd.), 0.5 mM $Co(NO_3)_2 \cdot 6H_2O$ (99.99% metals basis, Aladdin) and 0.8 mM $FeSO_4 \cdot 7H_2O$ (99.95% metals basis, Aladdin) in 0.25 M potassium borate ($K_2B_4O_7 \cdot 4H_2O$) buffer at pH 10. The photo-assisted electrodeposition was performed in a three-electrode configuration with Ag/AgCl as the reference electrode and a Pt wire as the counter electrode. The NiCoFe–B_i co-catalyst was electrodeposited onto the electrodes at a constant current density of 20 μA cm^{-2} over a period of 10 min under AM 1.5 G simulated sunlight. After the deposition, the electrodes were rinsed with deionized water.

Characterization methods

The morphologies and microstructures of the samples were characterized by field emission scanning electron microscopy (FESEM, JEOL, JSM-7800F, 15 kV) and transmission electron microscopy (TEM; FEI Talos F200X). Energy dispersive X-ray (EDX) spectroscopy elemental mapping was conducted under the TEM with an annular dark-field (ADF) detector. X-ray photoelectron spectroscopy (XPS) analysis was performed using a Thermo Scientific ESCALAB 250Xi instrument with monochromatic Al Kα radiation (225 W, 15 mA, 15 kV). All binding energies were referenced to the C 1s peak (284.8 eV) arising from adventitious carbon. The crystal phase was examined by powder X-ray diffraction (XRD, PANalytical X'Pert Powder with Cu Kα radiation). UV-visible (UV-vis) diffuse reflectance spectra were recorded on a UV-vis spectrophotometer (UV-3600, Shimadzu, Japan). Ultraviolet photoemission spectroscopy (UPS) measurements were carried out on an ESCALAB 250Xi spectrometer with He I resonance lines (21.22 eV). The steady-state photoluminescence (PL) spectra (excited by 420 nm illumination) were recorded on a spectrofluorometer (FLS1000, Edinburgh Instruments) equipped with both continuous (450 W) and pulsed xenon lamps. The time-resolved transient photoluminescence decay (TRPL) spectra were recorded on a spectrophotometer (Fluorolog-3, Horiba Scientific) using a 450 W xenon lamp. The surface photovoltaic properties (SPV) of the samples were tested using a surface photovoltage test system (CEL-SPS1000). The Ta, Cu and Zr concentrations in the Cu- and Cu,Zr_g-doped Ta_3N_5 were determined using inductively coupled plasma-atomic emission spectroscopy (ICP-AES; Icap 6300 Duo, Thermo Scientific). The oxygen and nitrogen contents of the synthesized Ta_3N_5 were determined using an oxygen–nitrogen combustion analyzer (Horiba, EMGA-620W).

Photoelectrochemical measurements

The PEC performance of the samples was investigated *via* a controllable reaction system (CEL-PAEM-D8, CEAULight, China) with a volume of approximately 150 mL. A commercial solar simulator (S500RE7, CEAULight, China) was used for irradiation of the photoanodes with a light intensity (1 sun at AM 1.5 G) of 100 mW cm^{-2}. The measurements were carried out in 1.0 M KOH (pH 13.6) aqueous solution under a three-electrode system on an electrochemical workstation (BioLogic SP-200). The temperature of the electrolyte was maintained at 10 °C using a constant temperature water bath during the PEC test. The as-prepared samples were used as the working electrodes (photoanode), Pt wire as the counter electrode, and a Hg/HgO electrode as the reference electrode, respectively. To prevent the back reaction and the light scattering effect of the generated H_2 bubbles, the Pt cathode chamber and the photoanode chamber were separated using a Nafion 117 membrane. The photocurrent was recorded under simulated solar light while sweeping the potential in the positive direction at a scan rate of 0.01 V s^{-1}. All the measured potentials *versus* a Hg/HgO reference electrode were converted to the potentials *versus* RHE according to the Nernst equation. The Applied Bias Photon-to-current Efficiency (ABPE) was calculated from the current–potential curves under AM 1.5 G illumination using the equation $ABPE = [J \times (1.23 - V_{app})/P_{light}] \times 100\%$, where V_{app} is the applied potential *versus* RHE, J is the photocurrent density under AM 1.5 G light and P_{light} is the irradiance of the simulated sunlight (100 mW cm^{-2}). The incident photoelectron conversion efficiency (IPCE) for each wavelength was determined using the following formula: $IPCE = (1240J)/(\lambda I_{light}) \times 100\%$, where λ is the wavelength of incident light (nm), J is the photocurrent density (mA cm^{-2}) under the illumination wavelength (λ), and I_{light} is the intensity of incident light (mW cm^{-2}). The IPCE spectra were measured using a monochromatic light source (PLS-SXE300) in the wavelength range from 360 to 650 nm with a 10 nm interval at 1.0 V *versus* RHE in 1 M KOH. The intensity of the monochromatic light was measured using a calibrated reference cell (CEL-FZ-A). Chronoamperometry measurements (steady-state photocurrent curves) were carried out at a potential of 1.0 V *versus* RHE under AM 1.5 G simulated sunlight (100 mW cm^{-2}). Electrochemical impedance spectra (EIS) were collected on the workstation at an open-circuit voltage under light illumination in a frequency range from 0.1 Hz to 100 kHz. Mott–Schottky plots were obtained at an AC frequency of 1.0 kHz at an amplitude of 0.01 V in the dark. Gas production was detected using a gas chromatograph (Aulight GC-7920) equipped with a thermal conductivity detector (TCD) and a flame ionization detector (FID).

Results and discussion

In order to determine the optimal doping levels of Cu and Zr for subsequent experiments, we first measured the oxygen production of photoanodes with different heteroatom doping amounts. The amounts of oxygen produced by NiCoFe–B_i/Cu–Ta_3N_5/FTO and NiCoFe–B_i/Zr–Ta_3N_5/FTO photoanodes, which were held at 1.0 V_{RHE} in 1 M KOH under AM 1.5 G simulated sunlight for 1 h, are shown in Fig. S1.† The figure displays a volcano-like shape and reveals that the optimal doping level ratios of Cu and Zr are ~6.4% and ~0.9%, respectively. Therefore, these two values were used as the doping levels for subsequent experiments. It is difficult to achieve gradient

doping using the most commonly employed synthesis method, normal atmospheric nitridation (Fig. S2†). In order to realize gradient doping, a simplified linear pressurized gas-assisted process can be used.[40,41] High-angle annular dark-field scanning transmission electron microscopy (HAADF-TEM) was employed to study the morphology and elemental distribution of Cu,Zr_g–Ta_3N_5. The morphology of Cu,Zr_g–Ta_3N_5 (Fig. 1a) is more compact than that of pristine Ta_3N_5 (Fig. S3†). The elemental mapping of Cu,Zr_g–Ta_3N_5 shows that Ta, N and Cu are uniformly distributed in the nanoparticles, while the distribution of Zr gradually increases from the inside to the outside. The line-scan EDS profile (Fig. 1e) results obtained along the cyan dotted-line from the Cu,Zr_g–Ta_3N_5 nanoparticles (Fig. 1a) are consistent with the elemental mapping images. As shown in Fig. 1b, the observed lattice fringes with an interplanar spacing of 0.366 nm were assigned to the (110) plane of Ta_3N_5.

As shown in Fig. 1c, the crystal structures of the Cu,Zr_g–Ta_3N_5 nanoparticles and control samples (pristine Ta_3N_5, Cu–Ta_3N_5) were characterized by X-ray diffractometry. All the samples show diffraction patterns consistent with a single phase of Ta_3N_5 (JCPDF no. 79-1533), which indicates that the crystal structure was not changed by Cu or Cu,Zr co-doping. More importantly, Cu_2O, ZrO_2, $ZrON_2$ and $NaTaO_3$ impurity phases were not observed in our sample. Furthermore, carefully examining the magnified diffraction peaks of the (110) facet (Fig. 1d) reveals a shift in the diffraction peaks to lower angles for all samples. The shifts in the (110) XRD peak positions of the various Ta_3N_5 are ascribed to the substitution of Ta^{5+} (radius: 64 pm^6) by Ta^{3+} (72 pm^6)/Cu^{2+} (73 pm^6)/Zr^{4+} (72 pm^6) as well as the substitution of N^{3-} (146 pm^6) by O^{2-} (140 pm^6). Substitutions of atoms with a larger ionic radius would shift the XRD peak position to a lower angle, while a smaller radius would result in a shift to a higher angle, respectively. The lower angle of the (110) peak generated by the pristine Ta_3N_5 compared with that of the standard is primarily due to the presence of Ta^{3+} ions. A shift in the (110) peak to lower angle presented in Cu–Ta_3N_5 compared with pristine Ta_3N_5 is due to the foreign cations (*i.e.*, Cu^{2+} ions) incorporated into Cu–Ta_3N_5. However, the angle shift of Cu–Ta_3N_5 is very small compared to that of pristine Ta_3N_5, which may be due to Cu–Ta_3N_5 containing more O_N defects compared to pristine Ta_3N_5. Cu,Zr_g–Ta_3N_5 displays the same (110) peak position as pristine Ta_3N_5, most probably as a result of the formation of a greater number of O_N defects in the former (Tables S1 and S3†). In addition, studies in the literature have proven that O_N can increase the carrier concentration and promote carrier transfer,[3,39] thus more O_N in samples will improve PEC performance. Meanwhile, the diffraction peaks of Cu,Zr_g–Ta_3N_5 become narrower and of higher intensity than both those of Cu–Ta_3N_5 and pristine Ta_3N_5, suggesting that the gradient incorporation of Zr enhanced crystallinity. The grain size obtained by applying the Scherrer equation to the (110) peak of Cu,Zr_g–Ta_3N_5 is the largest of all the samples (Table S4†).[42] Studies in the literature have confirmed that the grain

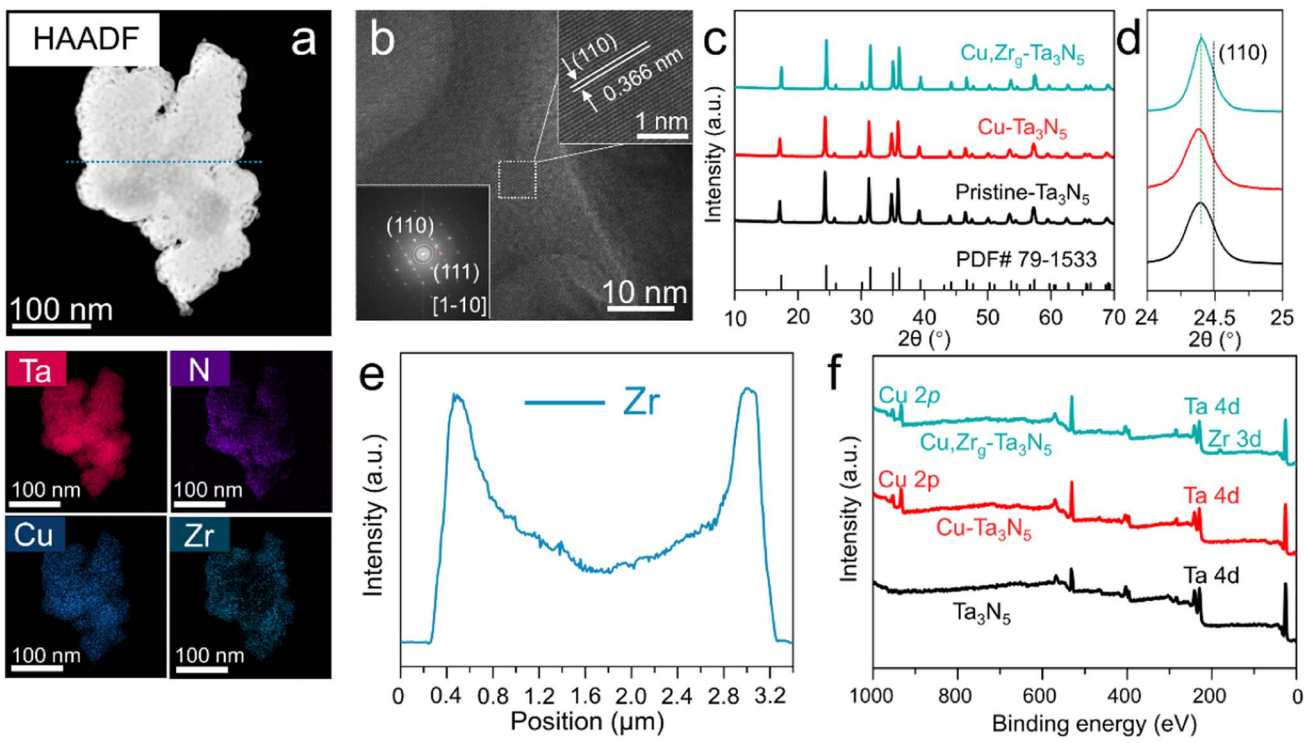

Fig. 1 (a) HAADF-STEM image of Cu,Zr_g–Ta_3N_5 and the corresponding EDS elemental mappings images of Cu,Zr_g–Ta_3N_5; (b) HRTEM images of Cu,Zr_g–Ta_3N_5 and the corresponding FFT pattern; (c) XRD spectra of Ta_3N_5, Cu–Ta_3N_5 and Cu,Zr_g–Ta_3N_5; (d) the zoomed-in image of Ta_3N_5, Cu–Ta_3N_5 and Cu,Zr_g–Ta_3N_5 (110) diffraction peaks; (e) the corresponding line-scan EDS profile obtained along the cyan dotted-line from (a); (f) wide-scan survey XPS profiles of Ta_3N_5, Cu–Ta_3N_5 and Cu,Zr_g–Ta_3N_5.

size of thin films affects PEC properties.[43] However, subsequent PEC testing in this study confirmed that the grain size of nanoparticles also affects the performance. The XPS wide-scan spectrum shows the apparent signals of the elemental Cu and Zr (Fig. 1f). The presence of Cu and Zr ions was verified from the high-resolution XPS spectra of samples (Fig. S4 and S5†). The presence of Ta^{3+} ions was verified from the Ta 4f XPS spectrum of pristine Ta_3N_5 (Fig. S7†).

We synthesized Cu,Zr_g–Ta_3N_5 nanoparticles using a simplified linear pressure-assisted method. The Cu,Zr_g–Ta_3N_5 nanoparticles exhibited a distinct morphology compared to pristine Ta_3N_5, Cu–Ta_3N_5, Zr–Ta_3N_5 and Cu,Zr_h–Ta_3N_5. As presented in Fig. 2a–e, pristine Ta_3N_5, Cu–Ta_3N_5, Zr–Ta_3N_5 and Cu,Zr_h–Ta_3N_5 show porous structures compared to Cu,Zr_g–Ta_3N_5. It is worth noting that the morphologies of Zr–Ta_3N_5 and Cu–Ta_3N_5 are similar to that of pristine Ta_3N_5, indicating that doping Cu or Zr alone do not change the morphology of Ta_3N_5. The morphology of Cu,Zr_h–Ta_3N_5, however, is different to those of pristine Ta_3N_5 and Ta_3N_5 doped with Cu or Zr alone, and it can be seen that the number of holes decreases (Fig. 2e). This is because interstitially doped Cu acts as an anchor point, and after Zr doping, interaction between Cu and Zr occurs due to the difference in electronegativity.[44] Nevertheless, the morphology of Cu,Zr_h–Ta_3N_5 is also different from that of Cu,Zr_g–Ta_3N_5. The morphology disparity observed between Cu,Zr_g–Ta_3N_5 and Cu,Zr_h–Ta_3N_5 particles can be attributed to the gradient doping of Zr, which gradually enhances the interaction between Zr and Cu from the outside in. This results in Cu,Zr_g–Ta_3N_5 exhibiting a denser morphology compared to the other samples. The Brunauer–Emmett–Teller (BET) test results further corroborate that Cu,Zr_g–Ta_3N_5 has fewer pores and its morphology is different from the other samples (Fig. 2f).

High-resolution X-ray photoelectron spectroscopy (XPS) data were employed to elucidate the valence states and chemical environment of the as-synthesized materials. The high-resolution Cu 2p spectra are exhibited in Fig. S4.† Notably, Fig. S4† reveals an interesting finding that Cu is present in the sample not only in the form of Cu^{2+}, but also as Cu^{+}. The presence of Cu^{+} in all Cu-doped Ta_3N_5 can be explained by the oxidation of Ta^{3+} ions by Cu^{2+}, which is why Ta^{3+} disappears when Ta_3N_5 is doped with Cu. However, the content of Cu^{+} is reduced and Cu^{2+} increased when Zr is incorporated into Cu–Ta_3N_5, regardless of uniform or gradient doping. This phenomenon can be explained by the difference in electronegativity, which causes electrons to transfer from Cu^{+} (1.163) to Zr^{4+} (1.610).[45] Electron transfer was further confirmed by the presence of Zr^{3+} in the Zr 3d XPS spectrum etched for 0 s (Fig. S5a†). We further performed XPS depth-profile analysis of Cu,Zr_g–Ta_3N_5 by means of argon sputtering, as shown in Fig. S5b and S6.† With an extension in the sputtering time, the peak area ratio of Zr^{3+} first increases and then decreases, while the peak area of Zr^{3+} in Cu,Zr_h–Ta_3N_5 remains almost unchanged (Fig. S8†). This proves that the interaction between Cu and Zr is continuously enhanced. The O 1s XPS spectra in Fig. S7a† show two typical peaks at approximately 530.2 and 531.4 eV, which are attributed to lattice oxygen (TaO_x species) and a surface-absorbed oxygen species, respectively.[34] The Ta 4f peak could be fitted to three doublets (Ta $4f_{7/2}$–Ta $4f_{5/2}$) with a spin–orbit splitting of 1.9 eV and a fixed area ratio of 4 : 3 (Fig. S7b†). The binding energy of the Ta $4f_{7/2}$ components were 23.6, 24.5, 26.0 eV, corresponding to Ta^{3+}, Ta_3N_5 and tantalum oxynitride (TaO_xN_y).[46] The proportions of Ta^{3+}, Ta_3N_5 and TaO_xN_y among the total Ta species in pristine Ta_3N_5 were estimated to be 12.5%, 85.8% and 1.7%, respectively. However, with Cu or Cu/Zr doping, the Ta^{3+} completely disappears, and

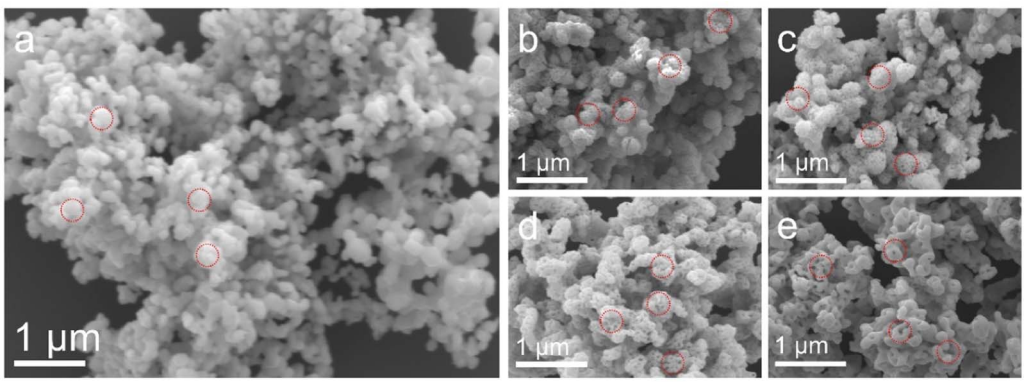

f

Samples	Ta_3N_5	Cu-Ta_3N_5	Zr-Ta_3N_5	Cu,Zr_h-Ta_3N_5	Cu,Zr_g-Ta_3N_5
BET surface area, $m^2\ g^{-1}$	10.0	9.6	9.8	6.5	4.8

Fig. 2 SEM images of (a) Cu,Zr_g–Ta_3N_5; (b) pristine Ta_3N_5; (c) Cu–Ta_3N_5; (d) Zr–Ta_3N_5 and (e) Cu,Zr_h–Ta_3N_5; (f) BET surface area of pristine Ta_3N_5, Cu–Ta_3N_5, Zr–Ta_3N_5, Cu,Zr_h–Ta_3N_5, and Cu,Zr_g–Ta_3N_5. In the same size red circle, (b–d) exhibit more pores than (e), but (e) shows more pores than (a).

the proportion of Ta_3N_5 is considerably increased (Table S3†). The N 1s peak at ~396.6 eV in Fig. S7c† corresponds to Ta–N binding. Additionally, a shift in the peaks of Cu–Ta_3N_5 and Cu,Zr_g–Ta_3N_5 is observed, demonstrating Cu or Cu/Zr have successfully doped.

To investigate the impact of Cu or Cu/Zr doping on the band gap structure, ultraviolet photoelectron spectroscopy (UPS) and ultraviolet-visible (UV-vis) spectroscopy were conducted to manifest the band edge positions of pristine Ta_3N_5, Cu–Ta_3N_5 and Cu,Zr_h–Ta_3N_5. By subtracting the cut-off energies for the secondary electrons from the He I excitation energy (21.22 eV), the Fermi levels (E_F) of pristine Ta_3N_5, Cu–Ta_3N_5 and Cu,Zr_h–Ta_3N_5 are −3.92, −4.10 and −4.37 eV, respectively (Fig. 3a). The UPS spectra reveal that the valence bands of pristine Ta_3N_5, Cu–Ta_3N_5 and Cu,Zr_h–Ta_3N_5 are 2.05, 1.89 and 1.94 eV below their Fermi levels, respectively (Fig. 3b). The UV-vis results show that the absorption of Cu–Ta_3N_5 and Cu,Zr_h–Ta_3N_5 is weaker than that of pristine Ta_3N_5 when the wavelength exceeds 600 nm (Fig. 3c). This is indicative of a lower density of defects caused by the reduced Ta^{5+} species or nitrogen vacancies.[47] The Tauc plots of the UV-vis spectra in Fig. 3d manifest that the optical band gaps of the pristine Ta_3N_5, Cu–Ta_3N_5 and Cu,Zr_h–Ta_3N_5 are 2.06, 2.08 and 2.10 eV, respectively. The low-valence cations (Cu^{2+} and Zr^{4+}) doped in Ta_3N_5 would require the formation of V_N and/or O_N (Table S1†) to compensate for the imbalanced charge.[48,49] Therefore, the valence band may partially be hybridized with O 2p orbitals with a lower electronic potential, leading to the enlarged band gap after Cu or Cu/Zr doping.[50] Combined with the UV-vis, UPS and Tauc data, the energy band positions of the pristine-Ta_3N_5, Cu–Ta_3N_5 and Cu,Zr_h–Ta_3N_5 are shown in Fig. 3e, which are consistent with the M–S plot results (Fig. S9†). Detailed values are summarized in Table S2.† As shown in Fig. 3e, the Fermi energy level of Cu, Zr_h–Ta_3N_5 is much lower than those of pristine Ta_3N_5 and Cu–Ta_3N_5. This finding confirms that gradient doping can tailor the band structure, thereby enhancing carrier separation.[34,35] The photoluminescence (PL) emission spectra of pristine Ta_3N_5, Cu,Zr_h–Ta_3N_5 and Cu,Zr_g–Ta_3N_5 are shown in Fig. 3f. The pristine Ta_3N_5 exhibits a quenched characteristic PL peak between 700 and 850, which is attributed to a strong defect-related

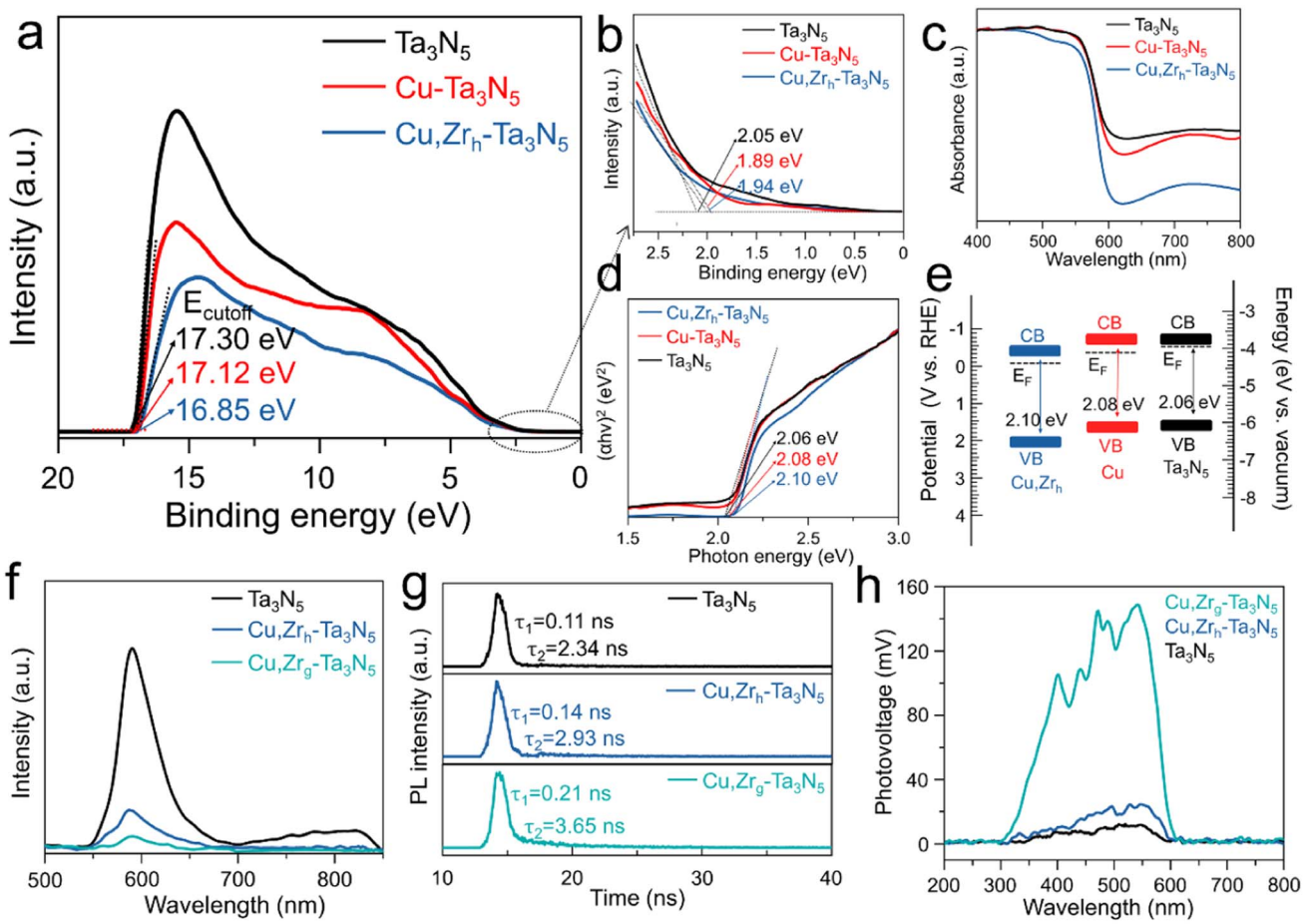

Fig. 3 (a) UPS spectra of Ta_3N_5, Cu–Ta_3N_5 and Cu,Zr_h–Ta_3N_5; (b) the zoomed-in image of the gray dashed line in (a); (c) UV-vis absorption spectra of Ta_3N_5, Cu–Ta_3N_5 and Cu,Zr_h–Ta_3N_5; (d) Tauc plots of the UV-vis absorption spectra of Ta_3N_5, Cu–Ta_3N_5 and Cu,Zr_h–Ta_3N_5. α, absorption coefficient; $\hbar$, Planck's constant; ν, photon frequency. The dotted lines show the extrapolation of the linear portion of the absorption edges; (e) band diagrams of Ta_3N_5, Cu–Ta_3N_5 and Cu,Zr_h–Ta_3N_5 determined from UPS and UV-vis absorption measurements. CB, conduction band; VB, valence band; E_F, Fermi level; (f) room temperature PL emission spectra of Ta_3N_5, Cu,Zr_h–Ta_3N_5 and Cu,Zr_g–Ta_3N_5; (g) TRPL decay curves of Ta_3N_5, Cu,Zr_h–Ta_3N_5 and Cu,Zr_g–Ta_3N_5; (h) SPV spectra of Ta_3N_5, Cu,Zr_h–Ta_3N_5 and Cu,Zr_g–Ta_3N_5.

recombination.[29] Notably, the disappearance of defect-related recombination in Cu,Zr_h–Ta_3N_5 and Cu,Zr_g–Ta_3N_5 confirms the positive effect of the Cu/Zr doping. The intensity of the PL emission spectrum, however, is significantly reduced after Zr gradient doping, indicating that the gradient Zr bends the band structure to facilitate the separation of photogenerated charges. Time-resolved PL (TRPL) spectroscopy was performed to study the carrier kinetics in various photoanodes (Fig. 3g). The fitted parameters for different Ta_3N_5 samples are listed in Table S5,† where τ_1 and τ_2 are the defect-related photogenerated carrier trapping and electron–hole recombination from the conduction band to the valence band, respectively.[51] As shown in Table S5,† the PL decay of the pristine Ta_3N_5 is mainly caused by defect-related recombination, while the defect-related recombination is slightly suppressed in Cu,Zr_h–Ta_3N_5. In contrast, both the τ_1 and τ_2 values of Cu,Zr_g–Ta_3N_5 are greater than those of pristine Ta_3N_5 and Cu,Zr_h–Ta_3N_5. Importantly, the decreased τ_1 ratio of Cu,Zr_g–Ta_3N_5 implies that gradient-doping of Zr further inhibits the defect-related recombination. In addition, the electron–hole recombination lifetime of Cu,Zr_g–Ta_3N_5 is much longer than that of pristine Ta_3N_5 and Cu,Zr_h–Ta_3N_5, suggesting that gradient doping with Zr improves carrier separation capability. We also used surface photovoltaic (SPV) spectral data to advance the understanding of the surface separation/transfer ability of carriers for different samples (Fig. 3h). The signal of Cu,Zr_g–Ta_3N_5 is markedly enhanced relative to those of Cu,Zr_h–Ta_3N_5 and pristine Ta_3N_5, indicating accelerated carrier separation/transfer of Cu,Zr_g–Ta_3N_5. The rapid carrier separation and transfer is conducive to the negative shift in the onset potential, which was confirmed in the subsequent PEC tests.

In response to the issue of the sluggish oxygen evolution kinetics of Ta_3N_5, a NiCoFe–B_i oxygen evolution co-catalyst layer was deposited on the surface of the photoelectrodes.[39,52] We deposited pure NiCoFe–B_i on FTO to demonstrate its excellent oxygen evolution reaction (OER) properties. As shown in Fig. S10,† NiCoFe–B_i/FTO exhibits excellent OER performance and stability. To advance our understanding of the importance of NiCoFe–B_i in the enhanced OER performance of Cu,Zr_g–Ta_3N_5, electrochemical-impedance-spectroscopy (EIS) and chopped *I–T* tests at 1.0 V_{RHE} were carried out. Obviously lower resistance between photoanode and electrolyte was observed, indicating that co-catalyst modification is necessary to enhance the charge transfer kinetics between the photoanode and electrolyte (Fig. S11†). Furthermore, the greatly enhanced photocurrent demonstrates the importance of NiCoFe–B_i in improving this property (Fig. S12†).[53,54] The SEM images of Cu,Zr_g–Ta_3N_5 deposited on FTO and NiCoFe–B_i adhering to Cu,Zr_g–Ta_3N_5 are shown in Fig. S13.† It can be seen that Cu,Zr_g–Ta_3N_5 is uniformly deposited on FTO, while NiCoFe–B_i is also uniformly adhered to Cu,Zr_g–Ta_3N_5. Due to the gradient bandgap structure resulting from the gradient doping of Zr in Cu,Zr_g–Ta_3N_5, electrons are able to transfer quickly to the surface of the photoanode to generate a photocurrent at a low bias (depicted in Fig. 4a). Steady-state photocurrent testing under low bias conditions was conducted (Fig. 4b). A steady photocurrent density of ~20 μA cm^{-2} was generated at 0.38 V_{RHE}, demonstrating a low onset potential for the Cu,Zr_g–Ta_3N_5 photoanode. To the best of our knowledge, this is better than the results of other Ta_3N_5-based photoanodes deposited on FTO (Fig. 4f). Linear-sweep voltammetry (LSV) was employed to study the PEC activity of Cu,Zr_g–Ta_3N_5, and the corresponding control sample results are also shown in Fig. 4c and S14a.† Apparently, the doping of foreign elements enhances the photocurrent density of Ta_3N_5. The fill factor of the *J–V* curves was also substantially improved. This phenomenon indicates that foreign ion doping significantly inhibits defect-related recombination, which is consistent with the PL and TRPL results. Compared to pristine Ta_3N_5 with a value of ~2.2 mA cm^{-2}, Cu–Ta_3N_5 and Cu,Zr_h–Ta_3N_5 exhibit values of ~6.5 mA cm^{-2} and ~6.7 mA cm^{-2}, respectively; however, Cu,Zr_g–Ta_3N_5 achieves the highest photocurrent density of ~8.9 mA cm^{-2} at 1.23 V_{RHE}. To the best of our knowledge, a photocurrent density of ~8.9 mA cm^{-2} is the highest value reported upon depositing Ta_3N_5 on FTO (Fig. 4f). Additionally, as shown in Fig. 4c and S14a,† compared to pristine Ta_3N_5, Ta_3N_5 doped with foreign ions exhibits a lower onset potential. The onset potential of Cu,Zr_h–Ta_3N_5 (~0.43 V_{RHE}) is negatively shifted compared to Cu–Ta_3N_5 (~0.5 V_{RHE}), which is due to the incorporation of Zr.[49] Notably, when Zr is gradient-doped into Cu–Ta_3N_5, not only is there a cathodic shift in the onset potential, but also the photocurrent density is significantly enhanced relative to that of Cu,Zr_h–Ta_3N_5. This can be ascribed to the gradient doping of Zr forming a gradient bend band structure that enhances carrier separation. Owing to the high photocurrent density, low onset potential and high fill factor, the Cu,Zr_g–Ta_3N_5 photoanodes reached a maximum ABPE of 3.5% (Fig. 4d and S14b†), which compares favorably with the previous literature on Ta_3N_5-based photoanodes, to the best of our knowledge.[34,55,56] This demonstrates the exceptional performance of Cu,Zr_g–Ta_3N_5 for PEC applications. Fig. S15† shows the IPCEs of pristine Ta_3N_5 and Cu,Zr_g–Ta_3N_5. The IPCE onset wavelength of pristine Ta_3N_5 and Cu,Zr_g–Ta_3N_5 are around 600 nm, corresponding to a band gap of ~2.1 eV. The value of Cu,Zr_g–Ta_3N_5 (maximum value 72%) is significantly higher than that of pristine Ta_3N_5, implying that gradient Zr doping enhances the charge carrier separation/transfer efficiency. The oxygen production of the Cu,Zr_g–Ta_3N_5 photoanode at 1.0 V_{RHE} under AM 1.5 G was determined by gas chromatography (Fig. 4e). The continuous evolution of oxygen with a faradaic efficiency (FE) of close to 100% manifests that the high and stable photocurrent is primarily used for oxygen production rather than for other side reactions.

Photoanode stability is another crucial criterion by which to evaluate the PEC performance. The stability of the Cu,Zr_g–Ta_3N_5 photoanode in 1 M KOH was tested under 1 sun at 1.0 V_{RHE} (Fig. 4g and S14c†). The steady-state photocurrent density was stable for 180 min for Cu,Zr_g–Ta_3N_5, which is consistent with the *J–V* curve at 1.0 V_{RHE} shown in Fig. 4c. The photocurrent density of Cu,Zr_g–Ta_3N_5 still remained at 86% of the initial value after 10 h (Fig. S16†). Although pristine Ta_3N_5, Cu–Ta_3N_5 and Cu,Zr_h–Ta_3N_5 demonstrated stable currents initially, their performance was not sustainable over time. After only 30 min, the photocurrent of pristine Ta_3N_5 abruptly dropped, while the stabilities of Cu–Ta_3N_5 and Cu,Zr_h–Ta_3N_5 were also limited to just 67 and 88 min, respectively. The stability of the Cu,Zr_g–Ta_3N_5 photoanodes after 3 h was studied in more detail. As shown in Fig. S17a,† there was no obvious change in XRD

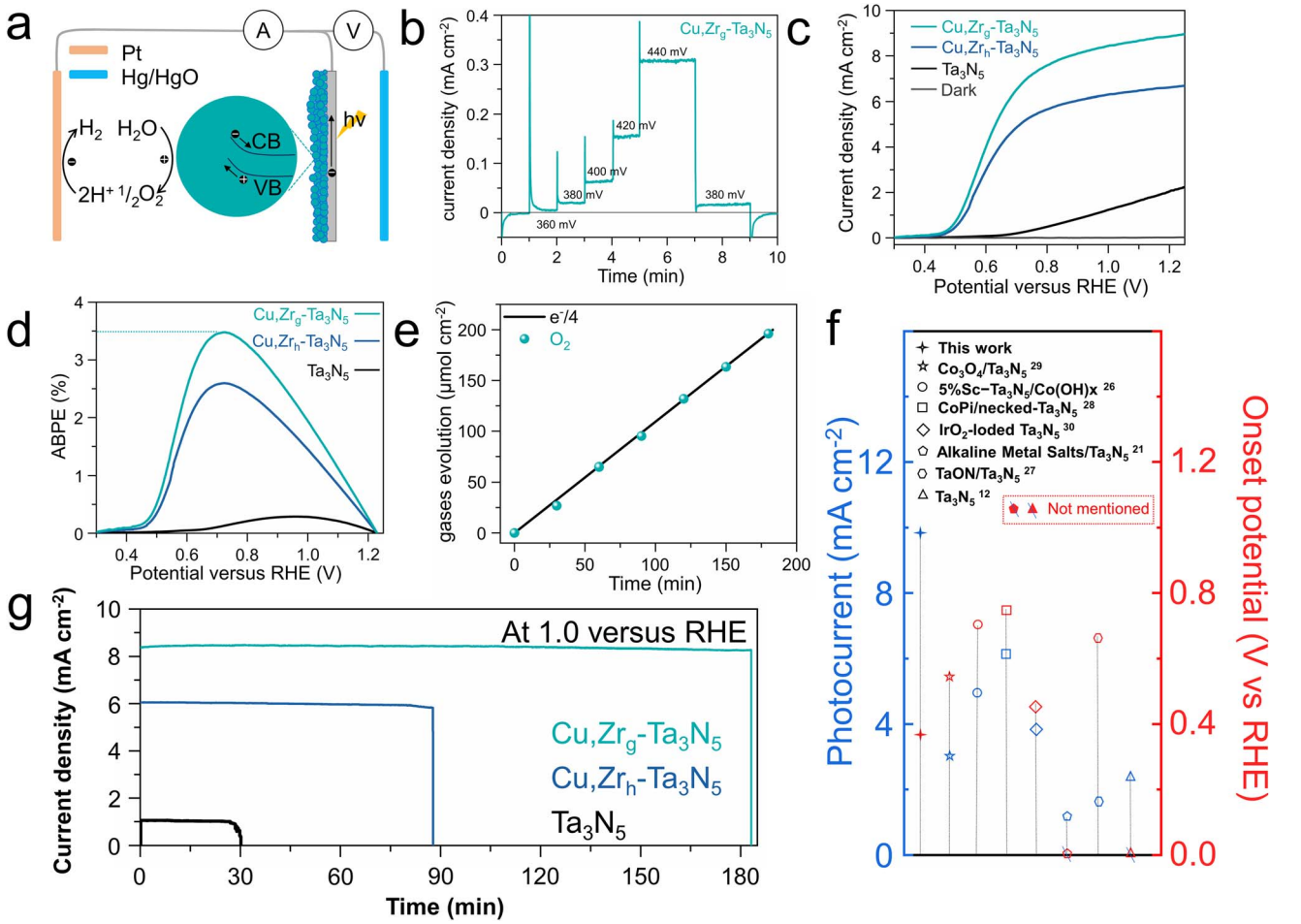

Fig. 4 (a) Schematic diagram of carrier migration and separation under simulated sunlight and bias; (b) steady-state photocurrent of the NiCoFe–B_i/Cu,Zr_g–Ta_3N_5/FTO photoanode under low applied potentials; (c) *J*–*V* curves of Ta_3N_5, Cu,Zr_h–Ta_3N_5 and Cu,Zr_g–Ta_3N_5 photoanodes with a NiCoFe–B_i co-catalyst in 1 M KOH under AM 1.5 G simulated sunlight; (d) ABPE of the photoanodes calculated from the *J*–*V* curves in (c); (e) amount of oxygen evolved from the NiCoFe–B_i/Cu,Zr_g–Ta_3N_5/FTO photoanode under an applied potential of 1.0 V *versus* RHE; (f) comparison of the photocurrent and onset potential between our NiCoFe–B_i/Cu,Zr_g–Ta_3N_5/FTO and other Ta_3N_5-based photoanodes deposited on FTO. The left vertical axis represents the photocurrent at 1.23 V_{RHE}, while the right vertical axis represents the onset potential of the comparison sample; (g) steady-state photocurrents of Ta_3N_5, Cu,Zr_h–Ta_3N_5 and Cu,Zr_g–Ta_3N_5 with a NiCoFe–B_i co-catalyst at 1.0 V *versus* RHE under AM 1.5 G simulated sunlight.

patterns, indicating that Cu,Zr_g–Ta_3N_5 exhibits excellent stability. The SEM image illustrates that Cu,Zr_g–Ta_3N_5 retains its morphology after stability testing (Fig. S17b†). The XPS results after the durability tests were not significantly different from those before the reaction, which also provided strong evidence for the stability of the photoanode (Fig. S18†). The outstanding structural stability of the Cu,Zr–Ta_3N_5 photoanodes may be attributed to two reasons: (1) Zr is co-doped with O_N;[44] (2) gradient doped Zr and interstitial doped Cu generate a gradually increasing interaction. Contrastingly, the XPS and SEM results of pristine Ta_3N_5 exhibit a clear chemical state change and structural collapse (Fig. S19 and S20†).

Conclusions

In summary, Ta_3N_5 nanoparticles with Cu and gradient Zr doping were prepared using a two-step method. We found that due to the difference in electronegativity, interstitially doped Cu acts as an anchor site to interact with Zr. Therefore, the morphology of the Cu,Zr_g–Ta_3N_5 becomes more compact, and the compact morphology reduces the combination rate of carriers at the grain boundaries, which is conducive to improving the PEC performance. In addition, as doping Zr can alter the band edge positions, a Zr gradient-doping method was proposed to modify the band structure of Ta_3N_5, which enhanced the separation of carriers. Due to the gradual increase in the doped Zr content from the inside out, the interaction between Zr and Cu increased from the outside in, resulting in a denser morphology of Cu,Zr_g–Ta_3N_5 compared to that of Cu,Zr_h–Ta_3N_5. The resultant Cu,Zr_g–Ta_3N_5 possesses superior structural stability and exhibits extraordinary PEC performance. The use of co-doping to modify the morphology and engineer the band structure paves the way for other nanoparticle semiconductor light absorbers to improve PEC performance.

Data availability

The data that support the findings of this study are available from the corresponding author upon reasonable request.

Author contributions

Xiaodong Wang and Huijuan Zhang conducted the project and contributed equally to this work. Chuanzhen Feng performed the photoelectrochemical tests. Yu Wang supervised the project and conceived the idea.

Conflicts of interest

The authors declare no conflict of interest.

Acknowledgements

This study was supported by the Fundamental Research Funds for the Central Universities (0301005202017, 2018CDQYFXCS0017, 106112017CDJXSYY0001), the Thousand Young Talents Program of the Chinese Central Government (Grant No. 0220002102003), the National Natural Science Foundation of China (NSFC, Grant No. 22371022, 22271029, U19A20100, 21971027, 21373280, 21403019), the Beijing National Laboratory for Molecular Sciences (BNLMS) and Hundred Talents Program at Chongqing University (Grant No. 0903005203205), the State Key Laboratory of Mechanical Transmissions Project (SKLMTZZKT-2017M11), the Natural Science Foundation of Chongqing (Grant No. cstc2019jcyj-msxmX0426), and the Science and Technology Research Project of Education Agency of Chongqing (Grant No. KJZD-K201800102).

References

1 Y. He, P. Ma, S. Zhu, M. Liu, Q. Dong, J. Espano, X. Yao and D. Wang, *Joule*, 2017, **1**, 831–842.
2 M. Volokh, G. Peng, J. Barrio and M. Shalom, *Angew Chem. Int. Ed. Engl.*, 2019, **58**, 6138–6151.
3 J. Fu, F. Wang, Y. Xiao, Y. Yao, C. Feng, L. Chang, C.-M. Jiang, V. F. Kunzelmann, Z. M. Wang, A. O. Govorov, I. D. Sharp and Y. Li, *ACS Catal.*, 2020, **10**, 10316–10324.
4 T. Higashi, H. Nishiyama, V. Nandal, Y. Pihosh, Y. Kawase, R. Shoji, M. Nakabayashi, Y. Sasaki, N. Shibata, H. Matsuzaki, K. Seki, K. Takanabe and K. Domen, *Energy Environ. Sci.*, 2022, **15**, 4761–4775.
5 Y. Qiu, Z. Liu, A. Sun, X. Zhang, X. Ji and J. Liu, *ACS Sustain. Chem. Eng.*, 2022, **10**, 16417–16426.
6 L. Zhang, L. Li, J. Liang, X. Fan, X. He, J. Chen, J. Li, Z. Li, Z. Cai, S. Sun, D. Zheng, Y. Luo, H. Yan, Q. Liu, A. A. Alshehri, X. Guo, X. Sun and B. Ying, *Inorg. Chem. Front.*, 2023, **10**, 2766–2775.
7 J. Chen, L. Zhang, J. Li, X. He, Y. Zheng, S. Sun, X. Fang, D. Zheng, Y. Luo, Y. Wang, J. Zhang, L. Xie, Z. Cai, Y. Sun, A. A. Alshehri, Q. Kong, C. Tang and X. Sun, *J. Mater. Chem. A*, 2023, **11**, 1116–1122.
8 K. Sivula and R. van de Krol, *Nat. Rev. Mater.*, 2016, **1**, 15010.
9 V. Nandal, Y. Pihosh, T. Higashi, T. Minegishi, T. Yamada, K. Seki, M. Sugiyama and K. Domen, *Energy Environ. Sci.*, 2021, **14**, 4038–4047.
10 W. Yang, R. R. Prabhakar, J. Tan, S. D. Tilley and J. Moon, *Chem. Soc. Rev.*, 2019, **48**, 4979–5015.
11 L. Jin, F. Cheng, H. Li and K. Xie, *Angew. Chem., Int. Ed.*, 2020, **59**, 8891–8895.
12 B. A. Pinaud, P. C. K. Vesborg and T. F. Jaramillo, *J. Phys. Chem. C*, 2012, **116**, 15918–15924.
13 M. Xiao, Z. Wang, B. Luo, S. Wang and L. Wang, *Appl. Catal., B*, 2019, **246**, 195–201.
14 L. Wang, X. Zhou, N. T. Nguyen, I. Hwang and P. Schmuki, *Adv. Mater.*, 2016, **28**, 2432–2438.
15 H. Hajibabaei, D. J. Little, A. Pandey, D. Wang, Z. Mi and T. W. Hamann, *ACS Appl. Mater. Interfaces*, 2019, **11**, 15457–15466.
16 M. Xiao, B. Luo, M. Lyu, S. Wang and L. Wang, *Adv. Energy Mater.*, 2017, **8**, 1701605.
17 T. Higashi, H. Nishiyama, Y. Suzuki, Y. Sasaki, T. Hisatomi, M. Katayama, T. Minegishi, K. Seki, T. Yamada and K. Domen, *Angew Chem. Int. Ed. Engl.*, 2019, **58**, 2300–2304.
18 P. Wang, C. Ding, Y. Deng, H. Chi, H. Zheng, L. Liu, H. Li, Y. Wu, X. Liu, J. Shi and C. Li, *ACS Catal.*, 2023, **13**, 2647–2656.
19 Y. Li, L. Zhang, A. Torres-Pardo, J. M. Gonzalez-Calbet, Y. Ma, P. Oleynikov, O. Terasaki, S. Asahina, M. Shima, D. Cha, L. Zhao, K. Takanabe, J. Kubota and K. Domen, *Nat. Commun.*, 2013, **4**, 2566.
20 G. Liu, J. Shi, F. Zhang, Z. Chen, J. Han, C. Ding, S. Chen, Z. Wang, H. Han and C. Li, *Angew Chem. Int. Ed. Engl.*, 2014, **53**, 7295–7299.
21 P. Wang, P. Fu, J. Ma, Y. Gao, Z. Li, H. Wang, F. Fan, J. Shi and C. Li, *ACS Catal.*, 2021, **11**, 12736–12744.
22 Y. Kado, R. Hahn, C.-Y. Lee and P. Schmuki, *Electrochem. Commun.*, 2012, **17**, 67–70.
23 Y. Kado, C. Y. Lee, K. Lee, J. Muller, M. Moll, E. Spiecker and P. Schmuki, *Chem. Commun.*, 2012, **48**, 8685–8687.
24 S. S. Ma, T. Hisatomi, K. Maeda, Y. Moriya and K. Domen, *J. Am. Chem. Soc.*, 2012, **134**, 19993–19996.
25 Y. W. Kim, S. Cha, I. Kwak, I. S. Kwon, K. Park, C. S. Jung, E. H. Cha and J. Park, *ACS Appl. Mater. Interfaces*, 2017, **9**, 36715–36722.
26 J. Fu, Z. Fan, M. Nakabayashi, H. Ju, N. Pastukhova, Y. Xiao, C. Feng, N. Shibata, K. Domen and Y. Li, *Nat. Commun.*, 2022, **13**, 729.
27 M. Zhong, T. Hisatomi, Y. Sasaki, S. Suzuki, K. Teshima, M. Nakabayashi, N. Shibata, H. Nishiyama, M. Katayama, T. Yamada and K. Domen, *Angew. Chem., Int. Ed.*, 2017, **56**, 4739–4743.
28 S. Chen, S. Shen, G. Liu, Y. Qi, F. Zhang and C. Li, *Angew. Chem., Int. Ed.*, 2015, **54**, 3047–3051.
29 L. Pei, B. Lv, S. Wang, Z. Yu, S. Yan, R. Abe and Z. Zou, *ACS Appl. Energy Mater.*, 2018, **1**, 4150–4157.
30 L. Pei, H. Wang, X. Wang, Z. Xu, S. Yan and Z. Zou, *Dalton Trans.*, 2018, **47**, 8949–8955.

31 Z. Wang, Y. Qi, C. Ding, D. Fan, G. Liu, Y. Zhao and C. Li, *Chem. Sci.*, 2016, **7**, 4391–4399.
32 M. Liao, J. Feng, W. Luo, Z. Wang, J. Zhang, Z. Li, T. Yu and Z. Zou, *Adv. Funct. Mater.*, 2012, **22**, 3066–3074.
33 M. Higashi, K. Domen and R. Abe, *Energy Environ. Sci.*, 2011, **4**, 4138.
34 Y. Xiao, C. Feng, J. Fu, F. Wang, C. Li, V. F. Kunzelmann, C.-M. Jiang, M. Nakabayashi, N. Shibata, I. D. Sharp, K. Domen and Y. Li, *Nat. Catal.*, 2020, **3**, 932–940.
35 F. F. Abdi, L. Han, A. H. Smets, M. Zeman, B. Dam and R. van de Krol, *Nat. Commun.*, 2013, **4**, 2195.
36 Y. Lin, Y. Xu, M. T. Mayer, Z. I. Simpson, G. McMahon, S. Zhou and D. Wang, *J. Am. Chem. Soc.*, 2012, **134**, 5508–5511.
37 Y. Wu, X. Liu, H. Zhang, J. Li, M. Zhou, L. Li and Y. Wang, *Angew Chem. Int. Ed. Engl.*, 2021, **60**, 3487–3492.
38 C. Wang, T. Hisatomi, T. Minegishi, M. Nakabayashi, N. Shibata, M. Katayama and K. Domen, *Chem. Sci.*, 2016, **7**, 5821–5826.
39 Y. Xiao, Z. Fan, M. Nakabayashi, Q. Li, L. Zhou, Q. Wang, C. Li, N. Shibata, K. Domen and Y. Li, *Nat. Commun.*, 2022, **13**, 7769.
40 W. Fu, Y. Wang, J. Hu, H. Zhang, P. Luo, F. Sun, X. Ma, Z. Huang, J. Li, Z. Guo and Y. Wang, *Angew Chem. Int. Ed. Engl.*, 2019, **58**, 17709–17717.
41 C. Feng, Y. Wu, Y. Fu, H. Zhang and Y. Wang, *Appl. Surf. Sci.*, 2022, **605**, 154810.
42 Y.-R. Chen, Y. Chen, P.-H. Chiu, P.-H. Hsiao and C.-Y. Chen, *ACS Appl. Nano Mater.*, 2022, **5**, 8962–8972.
43 S. Hwang, S. H. Porter, M. Li, R. Thorpe, A. B. Laursen, H. Gu, A. Safari, M. Greenblatt, E. Garfunkel and G. C. Dismukes, *J. Phys. Chem. C*, 2022, **126**, 5970–5979.
44 J. Wang, Y. Jiang, A. Ma, J. Jiang, J. Chen, M. Li, J. Feng, Z. Li and Z. Zou, *Appl. Catal., B*, 2019, **244**, 502–510.
45 K. Li and D. Xue, *J. Phys. Chem. A*, 2006, **110**, 11332–11337.
46 J. Xiao, J. J. M. Vequizo, T. Hisatomi, J. Rabeah, M. Nakabayashi, Z. Wang, Q. Xiao, H. Li, Z. Pan, M. Krause, N. Yin, G. Smith, N. Shibata, A. Bruckner, A. Yamakata, T. Takata and K. Domen, *J. Am. Chem. Soc.*, 2021, **143**, 10059–10064.
47 Z. Wang, Y. Inoue, T. Hisatomi, R. Ishikawa, Q. Wang, T. Takata, S. Chen, N. Shibata, Y. Ikuhara and K. Domen, *Nat. Catal.*, 2018, **1**, 756–763.
48 Y. Wang, D. Zhu and X. Xu, *ACS Appl. Mater. Interfaces*, 2016, **8**, 35407–35418.
49 J. Seo, T. Takata, M. Nakabayashi, T. Hisatomi, N. Shibata, T. Minegishi and K. Domen, *J. Am. Chem. Soc.*, 2015, **137**, 12780–12783.
50 T. Takata, G. Hitoki, J. N. Kondo, M. Hara, H. Kobayashi and K. Domen, *Res. Chem. Intermed.*, 2007, **33**, 13–25.
51 X. Wang, X. Liu, Y. Wu, Y. Fu, H. Zhang, M. Zhou and Y. Wang, *Appl. Catal., B*, 2023, **323**, 122182.
52 C. Feng, F. Wang, Z. Liu, M. Nakabayashi, Y. Xiao, Q. Zeng, J. Fu, Q. Wu, C. Cui, Y. Han, N. Shibata, K. Domen, I. D. Sharp and Y. Li, *Nat. Commun.*, 2021, **12**, 5980.
53 S. Wei, S. Chang, J. Qian and X. Xu, *Small*, 2021, **17**, 2100084.
54 K. Zhang, B. Jin, C. Park, Y. Cho, X. Song, X. Shi, S. Zhang, W. Kim, H. Zeng and J. H. Park, *Nat. Commun.*, 2019, **10**, 2001.
55 G. Liu, S. Ye, P. Yan, F. Xiong, P. Fu, Z. Wang, Z. Chen, J. Shi and C. Li, *Energy Environ. Sci.*, 2016, **9**, 1327–1334.
56 Y. Pihosh, T. Minegishi, V. Nandal, T. Higashi, M. Katayama, T. Yamada, Y. Sasaki, K. Seki, Y. Suzuki, M. Nakabayashi, M. Sugiyama and K. Domen, *Energy Environ. Sci.*, 2020, **13**, 1519–1530.